

# A numerical study of the hemodynamic effect of the aortic valve on coronary flow

Shaily Wald<sup>1,2</sup> · Alex Liberzon<sup>1</sup> · Idit Avrahami<sup>2</sup> 

Received: 25 January 2017 / Accepted: 5 September 2017 / Published online: 19 September 2017  
© Springer-Verlag GmbH Germany 2017

**Abstract** During diastole, coronary perfusion depends on the pressure drop between the myocardial tissue and the coronary origin located at the aortic root. This pressure difference is influenced by the flow field near the closing valve leaflets. Clinical evidence is conclusive that patients with severe aortic stenosis (AS) suffer from diastolic dysfunction during hyperemia, but show increased coronary blood flow (CBF) during rest. Transcatheter aortic valve implantation (TAVI) was shown to decrease rest CBF along with its main purpose of improving the aortic flow and reducing the risk of heart failure. Physiological or pathological factors do not provide a clear explanation for the increase in rest CBF due to AS and its decrease immediately after TAVI. In this manuscript, we present a numerical study that examines the impact of AS and TAVI on CBF during rest conditions. The study compares the hemodynamics of five different 2D numerical models: a baseline “healthy valve” case, two AS cases and two TAVI cases. The analysis used time-dependent computational fluid–structure interaction simulations of blood flow in the aortic root including the dynamics of the flexible valve leaflets and the varying resistance of the coronary arteries. Despite its simplifications, our 2D model succeeded to capture the major effects that dominate the hemodynamics in the aortic root and to explain the hemodynamic effect that leads to the changes in CBF found in in vitro and clinical studies.

**Keywords** Aortic valve · Coronary flow · Aortic stenosis · TAVI · FSI

✉ Idit Avrahami  
IditAv@Ariel.ac.il

<sup>1</sup> School of Mechanical Engineering, Tel Aviv University, 69978 Tel Aviv, Israel

<sup>2</sup> Department of Mechanical Engineering and Mechatronics, Ariel University, P.O. Box 3, 44837 Ariel, Israel

## 1 Introduction

The combination of aortic stenosis (AS) and coronary artery disease (CAD) requires special attention and often correlated with additional complications (Kelly et al. 1988; Rosenhek et al. 2010). About half of the patients with a severe degree of AS also suffer from severe CAD, where 30–40% of AS patients suffer from angina symptoms or risk of sudden cardiac death (Gould and Carabello 2003; Julius et al. 1997; Kupari et al. 1992; Marcus et al. 1982; Rosenhek et al. 2010), with the absence of any evidence of coronary artery lesion at angiography (Gould and Carabello 2003; Marcus et al. 1982). In most cases, angina is relieved immediately after aortic valve replacement (Rolandi et al. 2016; Wiegerinck et al. 2015), although hypertrophy regression may take months or even years to alleviate (Gould and Carabello 2003). More interestingly, clinical evidences report that during *rest* conditions, coronary blood flow (CBF) *increases* with AS severity (Burwash et al. 2008; Carroll and Falsetti 1976; Eberli et al. 1991; Hongo et al. 1993; Lumley et al. 2016; Rolandi et al. 2016). Patients with severe AS have shown a higher peak diastolic coronary flow velocity during rest conditions compared with normal subjects (Meimoun et al. 2012) and a linear correlation between AS gradients and higher rest CBF (Omran et al. 1996).

Considerable research efforts have been carried out to reveal the interplay between the different physiological, hemodynamic and pathological factors of valve performance on coronary perfusion. The rapid reduction in CBF during *hyperemia* for AS patients was attributed to several hemodynamic and physiological factors, among them are changes in the diastolic coronary filling phase (Bertrand et al. 1981; Gould and Carabello 2003; Rajappan et al. 2002), suction wave intensity (Broyd et al. 2013; Gould and Johnson 2016b; Lee et al. 2016), heart rate (HR) (Davies et al. 2011), oxygen

demand (Rajappan et al. 2003), coronary resistance (Ben-Dor et al. 2009, 2014), left ventricular (LV) ejection volume (Nobari et al. 2013) and myocardial stress (Camici et al. 2012; Meimoun et al. 2012; Petropoulakis et al. 1995). Other factors relate to characteristic pathological changes such as reduced capillary density and dysfunction (Ahn et al. 2016; Broyd et al. 2013; Zingone 2008), or reduced aortic distensibility in post-stenotic aortic dilatation (Stefanadis et al. 1988). However, recent studies (Lumley et al. 2016; Paradis et al. 2014) proved that reduced CBF during hyperemia in AS are mostly attributed to *physiological* factors due to the abnormal high LV workload and cardiac-coronary coupling and not by microvascular pathologies. The mechanisms underlying the increase in CBF during *rest* in AS patients with normal coronaries remain unclear.

This issue became even more critical since the introduction of transcatheter aortic valve implantation (TAVI) (Cao et al. 2015). In the case of valve replacement surgery, patients are often treated in parallel with major thoracotomy. However, in the current era of TAVI, arterial interventions are considered with care since they might lead to alterations in LV and right ventricular function and arterial hemodynamics (Davies et al. 2011). For example, recent ESC guidelines restrict revascularization before TAVI only for patients with a severe coronary stenosis ( $>70\%$ ) (Kolh et al. 2014; Stefanini et al. 2014). Nevertheless, the optimal means of defining CAD and the assessment of myocardial ischemia in AS patients are not clear (Danson et al. 2016; Scalone and Niccoli 2015). Therefore, an understanding of how the aortic valve affects coronary hemodynamics is becoming increasingly clinically relevant in determining how to manage this coexisting CAD and to distinguish pure arterial disease from indirect limited coronary perfusion due to valvular disease (Gould and Johnson 2016a; Sen and Davies 2015) and to allow better understanding of the role of valve leaflets dynamics on the CBF.

CBF is determined by a deriving gradient pressure between the aortic and the arterial pressure. The arterial pressure is maximal during systole due to the compression exerted on the coronary arteries during LV construction. Therefore, CBF mostly occurs during diastole when the myocardial muscle relaxes. Both the aortic pressure and the gradient at the coronary ostia are a direct result of AV function (Gould et al. 1976). In this study, we hypothesize that there is a hemodynamic mechanism, based on vortex location and timing, which correlates between the orifice area and the coronary flow. To understand this hemodynamic mechanism, numerical and experimental studies have been developed. The experimental study is undergoing and would be published in a future publication. This manuscript presents the numerical model and its results.

The numerical solution of the time-dependent blood flow across the aortic valve is considered an extremely challenging

problem (Bianchi et al. 2015). Such a numerical simulation requires a strong coupling between the time-dependent flow and the dynamics of the flexible leaflets. The response of the flexible leaflets depends not only on the complex unsteady patterns of the flow, but also on the details of the valve anatomy, tissue properties, and the dynamic motion of the heart walls, thus giving rise to a fully coupled, multiscale and multiphysics fluid–structure interaction (FSI) problem (Avrahami 2012). The healthy native aortic valves and roots have been widely studied experimentally and numerically. However, most of the studies that used FSI to simulate flow through the AV concentrate on the *systolic* characteristics of the valve and the flow and thus do not consider the coronary structures (e.g. Borazjani 2013; Ge and Sotiropoulos 2010; Gilmanov et al. 2015; Griffith 2012; Kopanidis et al. 2015; Le et al. 2013; Marom et al. 2012; McQueen and Peskin 2000; Nicosia et al. 2003; Sotiropoulos 2015; Sotiropoulos and Borazjani 2009). The inclusion of coronary arteries in a FSI model of the aortic root increases the complexity of the problem, since it requires modeling the time-dependent varying coronary resistance. Therefore, most of previous studies have not been able to generate sufficient models to evaluate the influence of AV configuration on CBF characteristics.

In addition, such a simulation requires a careful analysis of the leaflet closure dynamics, when the fluid domain is divided into two separate domains. This goes together with the known challenge of strongly coupled FSI analysis of unsteady and transitional flow taking place in a complex 3D geometry, including nonlinear flexible leaflets that undergo large deformation and unpredictable contact dynamics.

Nobari et al. (2013) describe a 3D FSI model of the aortic root and coronaries in which pressure boundary condition were imposed. They showed that stiffer leaflets resulted with lower CBF, when keeping the LV pressure constant. This result may imply of a lower stroke volume (and lower ejection velocity) for the AS cases. From their results, it may be concluded that in the few cases of *reduced* CBF due to AS, the dominant mechanism relies on reduced cardiac output (CO) due to increased paravalvular pressure (Ben-Dor et al. 2009, 2014).

Another mathematical model was suggested by Garcia et al. (2009). They used a 1-D lumped model to describe the effect of AS on CBF, incorporating coronary impedance, time-dependent LV, aortic and coronary pressure waves. The simulated CBF agreed with a series of clinical measurements of patients with AS and normal coronary angiograms. The results show that while keeping a constant CO, for patients with AS, the CBF increases under rest conditions, and it reduced during hyperemia. They explained the decrease in CBF during hyperemia mainly due to a decrease in the diastolic coronary filling phase. However, no hemodynamic analysis could be drawn from this 1D model.

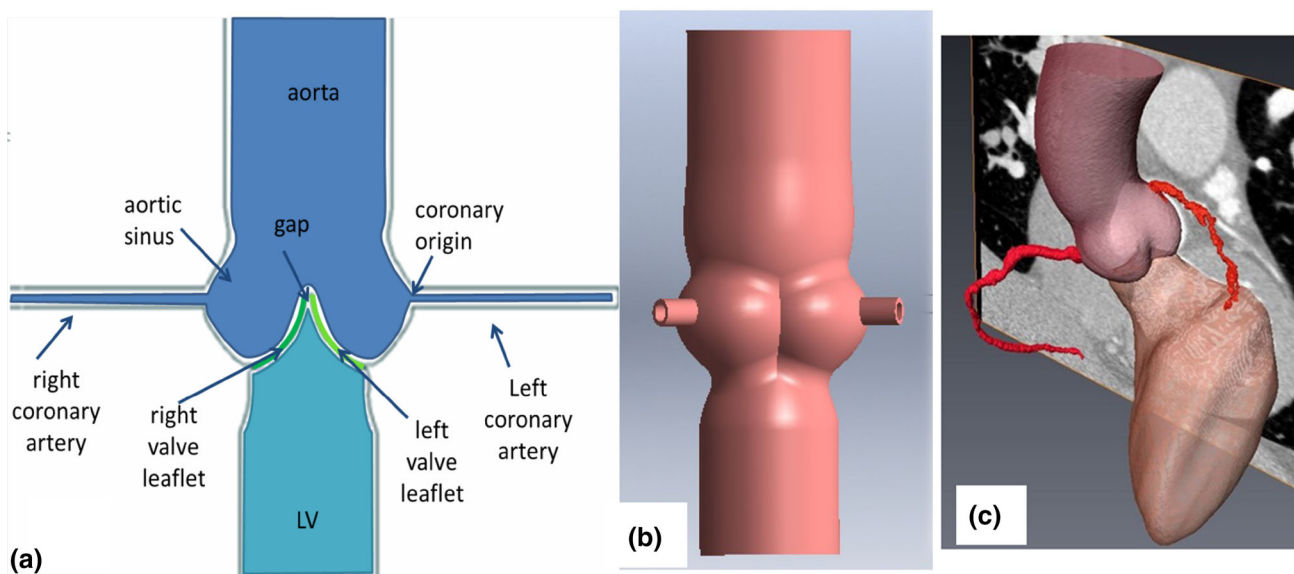


**Fig. 1** a The 2-D numerical model. b The 3D geometry of the experimental model

When it comes to the effect of TAVI design, the problem is even more complex. The challenge of developing the ideal aortic valve has created a wide range of investigative work over the last recent years. Some works are specifically related to the relationship between TAVI, the aortic valve, and the coronary hemodynamics. However, most of the studies concentrate in the systolic characteristics of the valve.

To the best of our knowledge, the impact of AS and TAVI on the coronary flow characteristics compared to a healthy valve has been largely unexplored. We focus on this aspect in the present work. In this study, we suggest a simplified 2D model which allows tracking the dominant features of flow in the aortic root and explain the main hemodynamic factors that dominant the CBF in healthy, AS and TAVI cases.

## 2 Methods

The numerical analysis included simulations of five different numerical models representing different cases of healthy, AS and TAVI cases. The models geometry included the aortic root, the leaflets and the coronary arteries. The time-depending simulations used *large deflection* FSI to incorporate the strong coupling between the leaflets and the flow, contact and gap features to allow *full closure of the valve* and lumped-model resistance to simulate the varying resistance of the coronary arteries. The simulations used the commercial package ADINA (ADINA R&D, Inc. v. 9.0.0)

### 2.1 The model geometry

The 2D geometry model of a normal aortic valve and root (Fig. 1a) was built based on a 3D experimental model

**Table 1** Highlighted model’s design parameters (specified in Fig. 2)

Model parameter	Acronyms	Value (mm)
Leaflet thickness	$L_T$	0.6
Inlet (LV) diameter	$D_L$	31
Sinotubular junction diameter	$D_{STJ}$	36
Healthy leaflet height	$h_L$	14.2
Coronary ostia diameter	$D_{LCO}$	7.4
Aortic valve base diameter	$D_B$	26
Left coronary height from the valve base	$h_{LCO}$	11.6
Leaflet length	$L_l$	19.6

(Fig. 1b), which was adapted from literature (Dvir et al. 2012, 2013) The experimental model was deliberately simplified to allow visualization measurements along central mid-planes (see “Appendix”). The model parameters were inspired by literature (Labrosse et al. 2006; Thubrikar 1989). The numerical model includes two fluid domains (proximal and distal to the leaflets). The distal domain includes the coronary arteries. Two flexible leaflets are represented by two solid domains (to calculate the leaflet motion).

Five different 2D geometrical models were built using the ADINA Modeler module. The inlet and outlet regions were extended to avoid interference of boundary conditions with the field of interest. Table 1 and Fig. 2 summarize the main design parameters of the different models. All models have similar geometric complexity, with specific modifications, as described in Table 2.

The flow was assumed to be laminar, and the blood was assumed incompressible and homogenous with density of  $\rho_f = 1100 \text{ kg/m}^3$  and Newtonian with dynamic viscos-

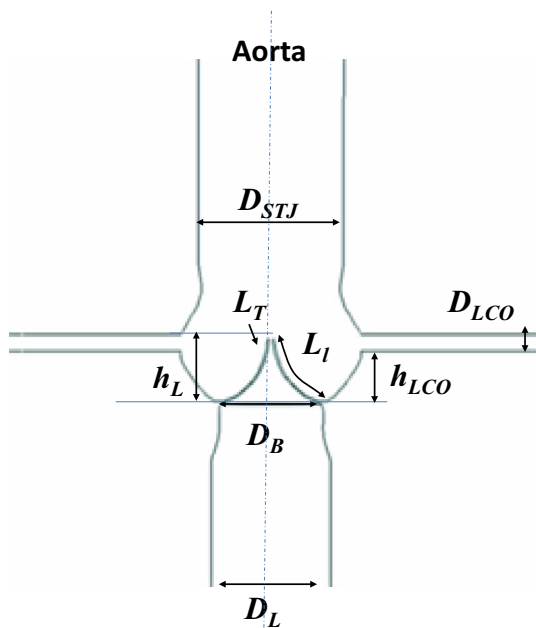


**Fig. 2** Highlighted design parameters of the model

ity of  $\mu = 0.0035 \text{ kg/ms}$  (Yoganathan et al. 2005). The leaflets were assumed to have isotropic and linear elastic properties with a Poisson's ratio of  $\nu = 0.45$ , density of  $\rho_s = 1123 \text{ kg/m}^3$  (Nobari et al. 2013) and Young's modulus of  $E = 4 - 40 \text{ MPa}$ , depending on the case (Grande-Allen et al. 2001). Table 2 and Fig. 3 detail the five different cases

studied, all conducted under the same physiological conditions. The five cases are: healthy model, two stenosis models (mild and severe) and two types of TAVI models (short and long). Valve stenosis was modeled by increased leaflet stiffness. According to literature, resistance to radial stretching of a calcified leaflet may increase 5–10 times than that of a normal healthy leaflet (Christie and Barratt-Boyes 1995; Miller et al. 2011; Weinberg et al. 2009). Seven different simulations were conducted for a range of stiffness from 4.5 MPa to 40. Finally, two representative cases were chosen to model mild and severe AS, with leaflet elasticity of 20 MPa and 40 MPa, respectively. The geometry of the long TAVI case was also built based on an experimental model, taking into consideration the dimensions of a typical commercially used TAVI valve implanted in the experimental model (see "Appendix"). The geometry of the short TAVI is similar to the long TAVI case, only with shorter leaflets. The TAVI models reflect the bio prosthesis skirt and the retracted native leaflets within the aortic annulus according to recommended valve implantations (Schultz et al. 2009; Dvir et al. 2013).

## 2.2 Governing equations

The flow and pressure fields in the fluid domains were calculated by solving the governing equations for the fluid domain for 2D, laminar, Newtonian and incompressible flow in a non-gravity field:

**Table 2** Summary of parameters for the investigated cases

Case name	Healthy case	Mild stenosis	Severe stenosis	Short TAVI	Long TAVI
Leaflet elastic modulus (kPa)	4	20	40	4	4
Leaflet length (mm)	19.6	19.6	19.6	23	27
Leaflet height (mm)	14	14	14	20	23

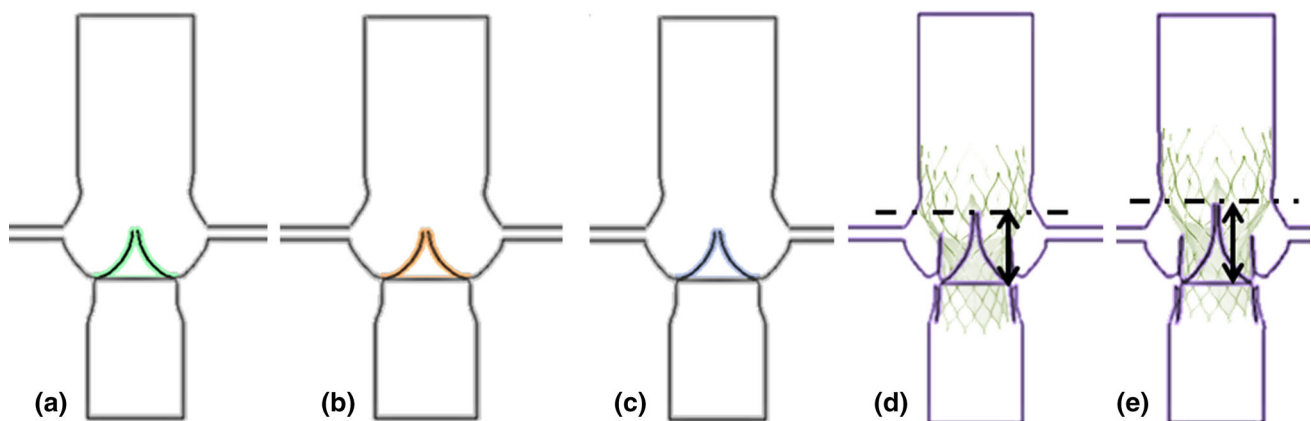


**Fig. 3** Geometric models of the five simulated cases: **a** healthy case, **b** mild stenosis with stiffness of 20 MPa, **c** severe stenosis with stiffness of 40 MPa, **d** short TAVI and **e** long TAVI

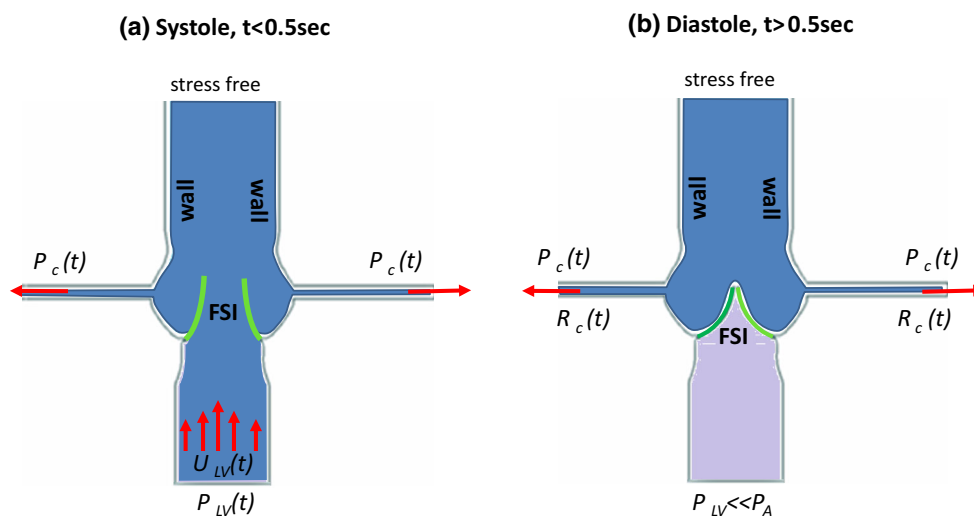


**Fig. 4** Applied boundary conditions on the fluid domain: At all time: stress-free conditions at the aorta (outlet), zero velocity (wall conditions) at the aortic and coronary wall, and FSI conditions at the interface with the leaflets. During systole **a** time-dependent velocity and pressure

at the LV inlet, time-dependent pressure at the two coronary outlets. During diastole **b** time-dependent pressure and resistance at the two coronary outlets, low LV pressure to ensure leaflets closure

$$\nabla \cdot \mathbf{U} = 0$$

$$\rho_f \left( \frac{\partial \mathbf{U}}{\partial t} + \mathbf{U} \cdot \nabla \mathbf{U} \right) = -\nabla P + \mu \cdot \nabla^2 \mathbf{U} \quad (1)$$

where  $P$  is the static pressure,  $\mathbf{U}$  is the velocity vector,  $t$  is time,  $\rho_f$  is fluid density and  $\mu$  is the dynamic viscosity.

The governing equation for the solid domain is the momentum conservation equation:

$$\rho_s \frac{\partial^2 \mathbf{d}_s}{\partial t^2} - \nabla \cdot \boldsymbol{\sigma}_s = \mathbf{f}_s \quad (2)$$

where  $\boldsymbol{\sigma}_s$  is the stress tensor,  $\mathbf{d}_s$  is the vector of structure displacement,  $\rho_s$  is the leaflet density and  $\mathbf{f}_s$  represents the body force applied on the structure.

### 2.3 Boundary conditions at the fluid and solid domains

The same boundary conditions were applied for the five models (Fig. 4). Similar to other studies (Kim et al. 2008; Nobari et al. 2013), the boundary condition at the ascending aortic outlet was set to be stress-free. During systole, prescribed velocity conditions were imposed at the LV inlet, reflecting a typical physiological waveforms of a normal healthy human with a HR of 60 BPM, CO of 3 liters/min, and 40/60 systolic to diastolic ratio, as shown in Fig. 5a (Berne and Levy 1986). During diastole, zero inlet velocity was defined. At the coronary outlets, a combined lumped-model coronary resistance and pressures (normal traction) were imposed as boundary conditions. This technically leaves the velocity profile unconstrained and allows it to self-establish (Klabunde 2011; Nobari et al. 2013). In order to prevent coronary back-

flow during systole, additional calibrated pressure difference constrain (i.e., normal traction) was assigned at the LV inlet during systole, based on a typical paravalvular pressure difference, as shown in Fig. 5b. The pressure and resistance boundary conditions defined at the coronaries (described in Fig. 6) are a result of trial and error iterations to obtain a typical physiological coronary flow (Berne and Levy 1986; Marn et al. 2012) for the healthy case (Fig. 7).

The solid components representing the valve leaflets are assumed to be free to move according to fluid forces and only fixed at their edges. To ensure full closure of the valve during diastole, a contact algorithm was employed between the two valve leaflets based on a frictionless and elastic contact model. It is employed on the normal traction ( $\tau_n^{IJ}$ ) and gap ( $g_n$ ) components of the two leaflets interfaces ( $I$  and  $J$ ) come in contact during the closing phase. This ensures that no elements overlapping, adhesion or collapsing, according to the contact conditions at the interface (ADINA R&D 2000):

$$g_n \geq d_g ; \quad \tau_n^{IJ} \geq 0 ; \quad g_n \tau_n^{IJ} = 0 \quad (3)$$

$d_g = 1$  mm is a small gap defined at the fluid domain which is used to connect or disconnect two fluid domain-sectored from the contact condition. When the gap condition is open, the two domains (above and below the valve) are connected, and fluid can flow across the gap. In this case, the fluid variables are continuous across the interface. When the gap condition is closed, the two domains are disconnected, and fluid cannot flow across the gap. These conditions prevent mesh distortions due to the large displacement during valve closure. A specific time function was used to determine the appropriate gap closing and opening times during the car-

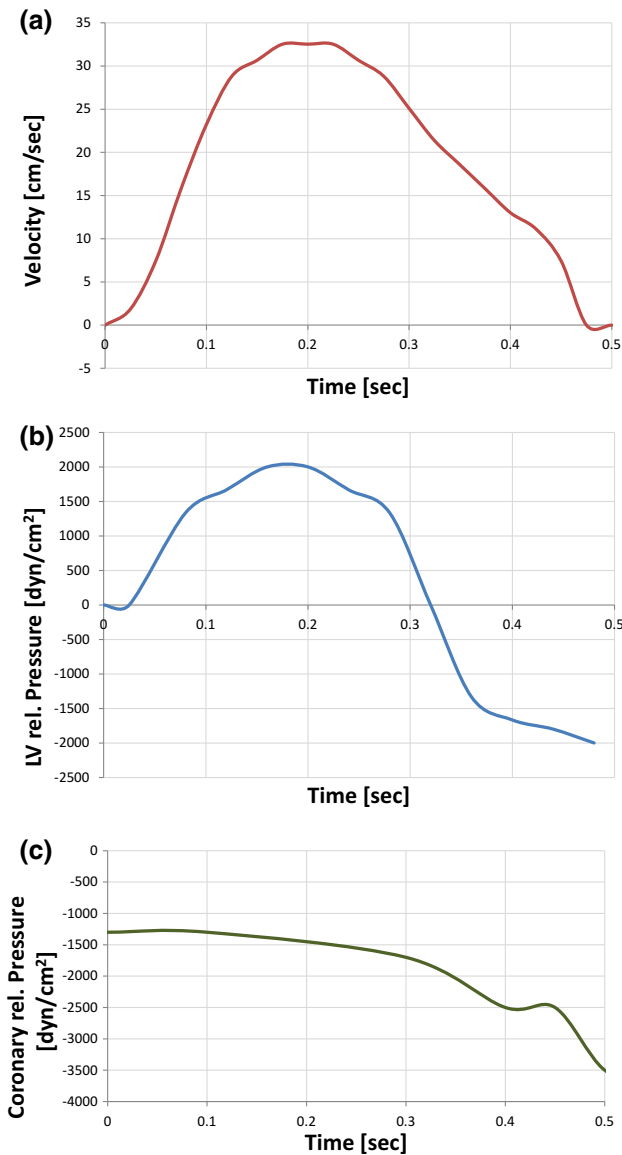


**Fig. 5** Time-dependent boundary conditions during systole ( $t < 0.5$  s). Upper chart **a** inlet LV velocity. Middle chart **b** inlet LV relative pressure (Normal Traction) condition. Lower chart **c** coronaries relative pressure (Normal Traction)

diac cycle. During the closing phase, the combination of gap and contact conditions acts similarly to a wall condition (no-slip\ no-penetration).

The boundary conditions on the FSI interfaces state that: (i) displacements of the fluid and solid domain must be compatible, (ii) tractions at these boundaries must be at equilibrium and (iii) fluid obeys the no-slip\ no-penetration conditions. These conditions are given in the follow equations:

$$\mathbf{d}_s = \mathbf{d}_f$$

$$\boldsymbol{\sigma}_s \cdot \hat{\mathbf{n}}_s = \boldsymbol{\sigma}_f \cdot \hat{\mathbf{n}}_f$$

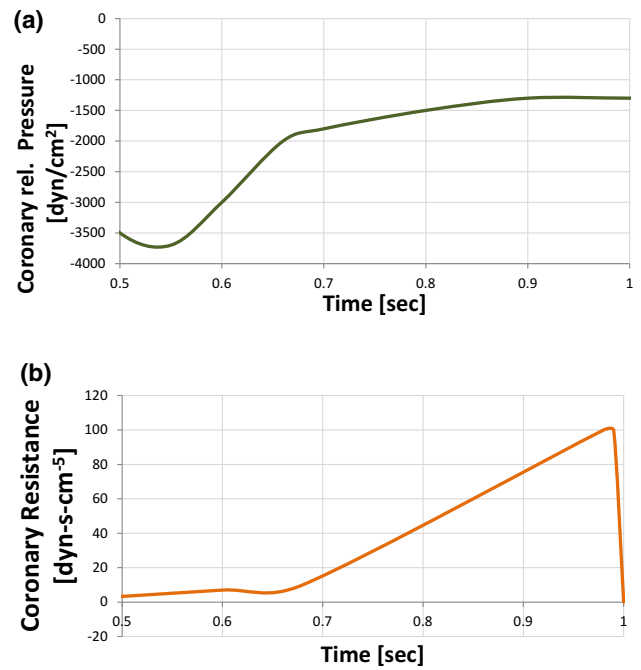


**Fig. 6** Time-dependent boundary conditions during diastole ( $t > 0.5$  s). Upper chart **a** coronaries relative pressure (Normal Traction). Lower chart **b** coronaries resistance

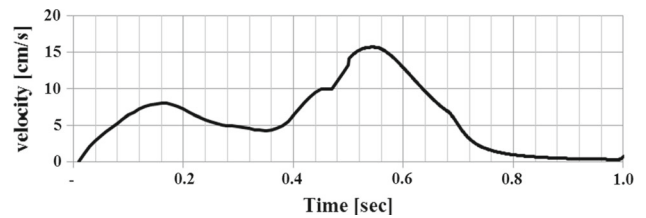


**Fig. 7** Resulted left coronary velocity for the healthy case

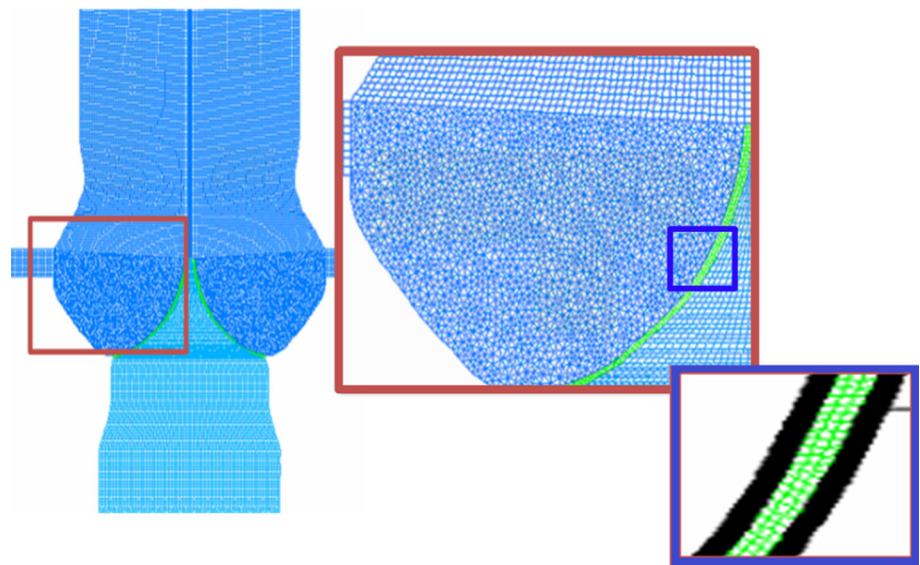
$$\dot{\mathbf{d}}_s = \mathbf{U}_f \tag{4}$$

where  $\boldsymbol{\sigma}$ ,  $\mathbf{d}$ ,  $\mathbf{U}$  and  $\hat{\mathbf{n}}$  are the stress tensors and displacement, velocity and boundary normal vectors, respectively, with the subscripts  $f$  and  $s$  indicating a property of the fluid and solid, respectively.

### 2.4 Numerical model

The governing equations of both the structure and fluid domains were solved using the finite element methods (FEM). The solid domain was meshed using  $\sim 900$  4-node quadrilateral plane strain elements. The fluid domain was meshed using a combination of 4-node quadrilateral and 3-node triangle plane elements, with total  $\sim 37,000$  linear flow-condition-based interpolation (FCBI) elements with mesh refinements near the boundaries. Figure 8 shows the mesh of the fluid (blue) and solid (green) domains with altogether more than 38,000 elements. Figure 9 shows the mesh

**Fig. 8** Fluid (blue) and solid (green) mesh domains. Red and blue rectangles represent magnified views of specific regions



of the TAVI cases. For mesh model validation test please refer to “Appendix”.

ADINA-FSI provides both *direct* and *iterative* FSI solvers. In the iterative FSI solvers, the fluid and solid domains of the model are solved sequentially, with information passed between them on the FSI boundaries, and therefore, it is advantageous in terms of memory requirements and CPU time. However, for our cases, which include strong coupling and large displacements, the iterative solver was not satisfactory, i.e., the solutions were unstable and failed to converge, while the direct FSI approach was shown to converge robustly. In this approach, the governing fluid and structural equations are solved simultaneously using one coefficient matrix (ADINA R&D 2000). Therefore, in our models we used the direct FSI approach. The direct approach is extremely computational demanding for CPU time and for access to spare memory and therefore limits the size of the mesh.

The FSI algorithm included models of large wall displacements and small strains. In order to control the moving mesh under large deformations of the flow domains, the arbitrary Lagrangian–Eulerian (ALE) approach was defined on geometric entities. ALE approach integrates the Eulerian description of the fluid domain with the Lagrangian formulation of the moving mesh using curvature correction (ADINA R&D 2000; Bathe 2006). Parallel leader–follower option was defined to control mesh adaptation to wall motion and overcome mesh distortion in the gap between leaflets. (ADINA R&D 2000).

The Newton–Raphson method was used to solve the nodal matrices (Doyle et al. 2010; Zhang and Bathe 2001). Time integration used altogether 551 time steps per cycle. A first-order Euler backward implicit time integration method

was used for the time marching. For time step validation tests see “Appendix”.

## 2.5 Parameters definitions

The velocity and flow to the coronary arteries are calculated based on the time-dependent average of the axial (streamwise) component velocity data ( $V_y$ ) extracted from a group of elements located at the left coronary ostia (shown in Fig. 9). The mean flow rate is computed as an integral along the cardiac cycle:

$$V_y = \frac{1}{A} \left( \int_A U_y dA \right) \quad (5)$$

$$Q = \frac{\pi d^2}{4} \int_{t=0}^{t=T} V_y dt \quad (6)$$

where  $V_y$  is the time-dependent average axial velocity,  $Q$  is the time integration flow rate,  $U_y$  is the time-dependent nodal velocity component at the streamwise direction,  $d$  is the artery diameter,  $A$  is the total area of the elements group and  $T$  is the cardiac period time.

Following Garcia et al. 2006, three pressure differences were defined for the hemodynamic analysis (shown schematically in Fig. 10). The left coronary flow is basically determined by those three pressure parameters:

- (i) The difference between LV pressure ( $P_{LV}$ ) and the aortic pressure ( $P_A$ ) is the net transvalvular pressure drop ( $TPG_{NET}$ )
- (ii) The difference between  $P_{LV}$  and the pressure at the left coronary inlet ( $P_{LC}$ ) is the maximal transvalvular pressure drop ( $TPG_{MAX}$ ) and is the driving pressure for the *systolic* coronary flow

**Fig. 9** Mesh of the TAVI model, with a magnified view (blue circle) of Elements group used for extraction of the mean velocity at the left coronary, marked as green element

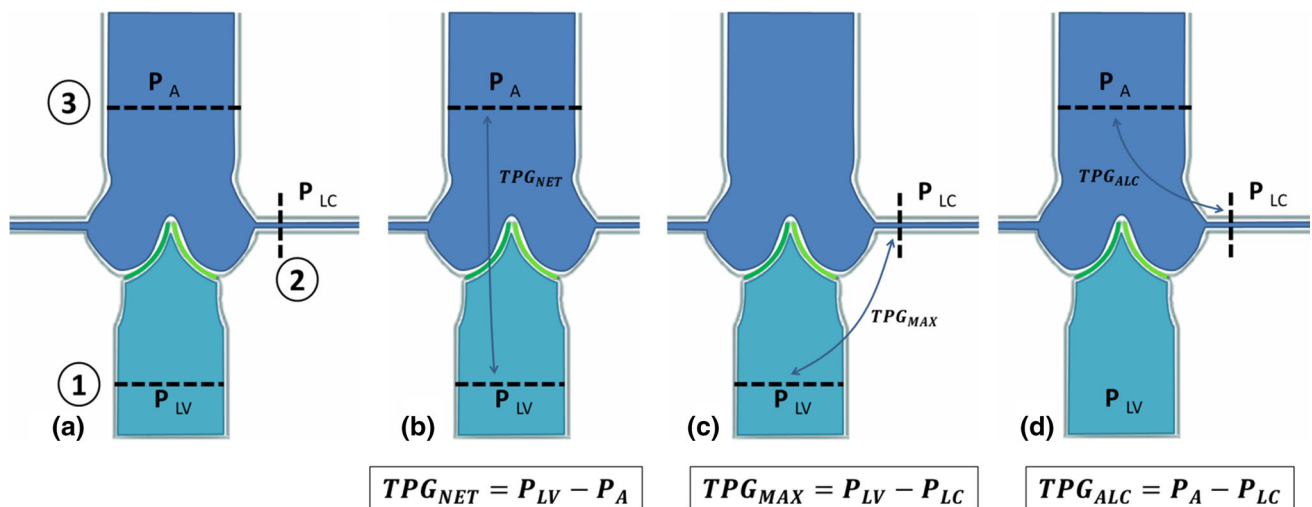
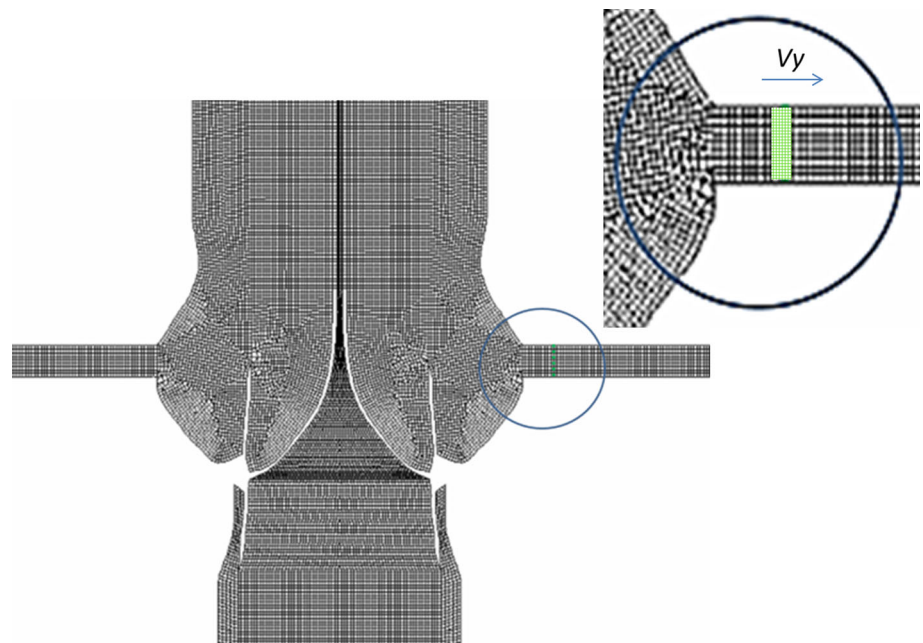


**Fig. 10** Pressure gradients definitions, **a** measurements locations in the models : (1) LV pressure  $P_{LV}$ , (2) left coronary inlet  $P_{LC}$ , (3) aortic pressure  $P_A$ . **b** net transvalvular gradient  $TPG_{NET}$ , **c** transcoronary gradient  $TPG_{MAX}$ , **d** coronary driving pressure  $TPG_{ALC}$

(iii) The pressures differences between  $P_A$  and  $P_{LC}$  is the aortic-coronary pressure drop ( $TPG_{ALC}$ ), which is the driving pressure for the *diastolic* coronary flow.

The pressure presented at each of these locations ( $P_A$ ,  $P_{LC}$  and  $P_{LV}$ ) are calculated as an average nodal pressure of element groups in the selected regions.

The AV effective orifice area (EOA) was calculated for each of the five models according to (Mahmood and Swaminathan 2010) using:

$$EOA = \frac{Q}{51.6\sqrt{TPG_{NET}}} \quad (7)$$

### 3 Results

Figure 11 shows the time-dependent coronary average velocity (calculated using Eq. 5) for all models. During systole, coronary vessels are compressed by the contracting heart muscle and thus the flow is low for all the cases with insignificant differences between them. During end systole, the coronary velocities decline. The healthy model (blue line) has the longest decline period (until  $t = 0.34$  s), while the severe AS case has the shortest decline period (until  $t = 0.25$  s). The mild AS case is delayed by 0.1 s after the severe AS case. Both of the TAVI models reach their minimum point after  $t = 0.26$  s. During the diastole phase, the coronary



**Fig. 11** Left coronary velocity, as calculated for all models during one cardiac cycle

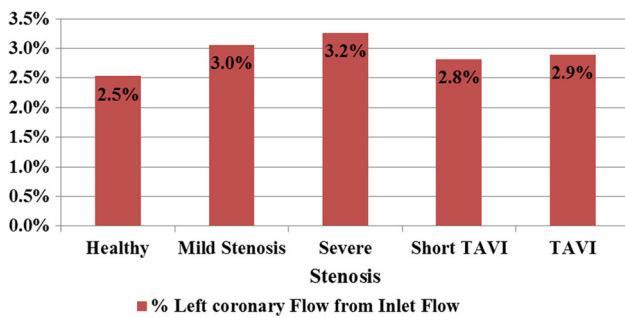
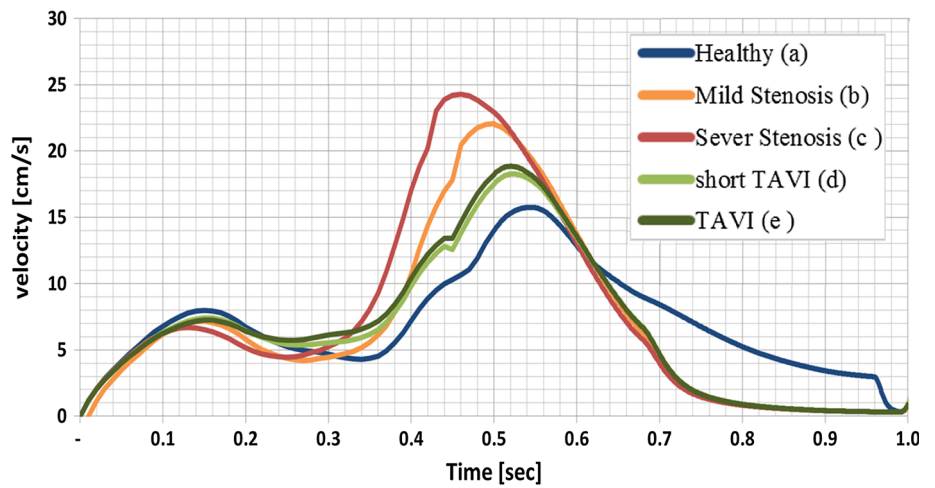


**Fig. 12** Left coronary flow rate expressed as percentage of the CO

flow resumes and the coronary flow reaches its maximum. At this time point, the differences between the cases are most profound. Both of the stenosis cases reach their maximum velocity at early stages of the diastole and with high velocity values. The severe AS case has the highest velocity value of 24 cm/s at  $t = 0.46$  s, whereas the mild AS case reaches a maximum of 22 cm/s at  $t = 0.5$  s. The healthy case, on the other hand, has the lowest velocity peak of only 15.7 cm/s

which takes place at  $t = 0.53$  s. Both of the TAVI cases reach about the same maximum velocity value of 18.5 m/s at  $t = 0.51$  s.

Figure 12 shows the time-integral coronary flow rate (calculated using Eq. 6) as a percentage of the CO along one cardiac cycle for the five models. The stenosis models have the highest percentage of flow through the left coronary, with 3.2% for the severe AS and 3% for the mild AS model. Both of the TAVI models present higher flow rates in the left coronary than the healthy model. The long TAVI has higher flow of 2.9%, and the short has 2.8% relative to the systolic CO. The healthy model has the lowest flow rate of only 2.5%.

During the systolic phase of the cardiac cycle, all cases represent a forward flow structure in the valve area which leads to the opening of the leaflets. Regardless of valve anatomy, the flow downstream of the leaflets is divided into two regions: (1) a jet originating from the valvular orifice and (2) a recirculation region flow marked by the presence of vortices located between the leaflet and the wall of the aortic sinus (Fig. 13). This recirculation is a result of the tip vortex ring forming due to the rolling of the developed shear layer.

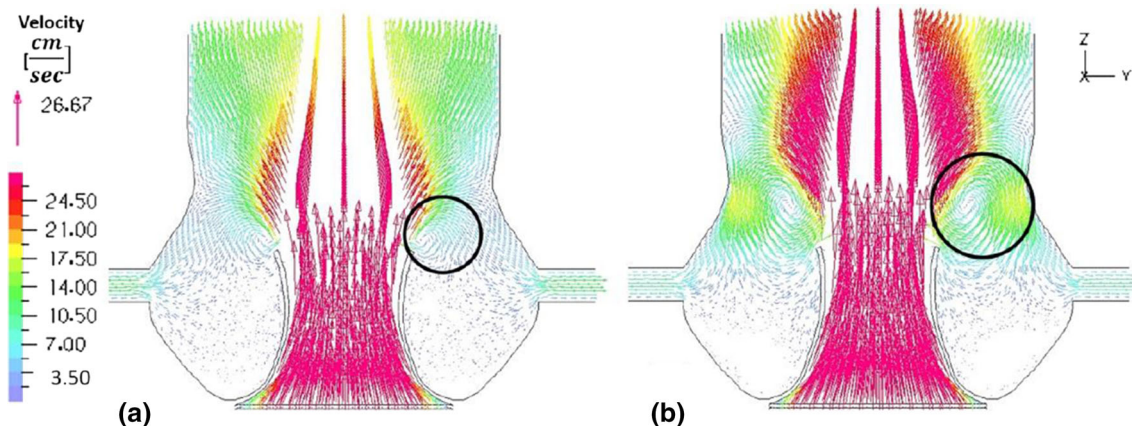


**Fig. 13** Vortices developed during systole (healthy case), marked by a black circle during valve closure phase **a** after 0.18 s, **b** after 0.22 s

**Table 3** Main hemodynamic results that influence the coronary flow in the five cases

Case	Healthy	Mild AS	Severe AS	Short TAVI	Long TAVI
Max. systolic orifice diameter (mm)	11	8.5	6.7	9.5	9.7
Calculated EOA (cm <sup>2</sup> )	1.8	1.17	1.11	1.63	1.65
Peak systolic velocity (cm/s)	60	83	95	70	75
Vortex location at $t = 0.26$ (mm)	38	53	59	45	49
Peak normalized $TPG_{ALC}$	0.02	0.44	0.79	0.23	0.33
Time of peak $TPG_{ALC}$ (s)	0.56	0.41	0.4	0.5	0.48
$CBF$ (ml/min)	76	91	98	84	87
$CBF/CO$ (%)	2.5	3.1	3.3	2.8	2.9

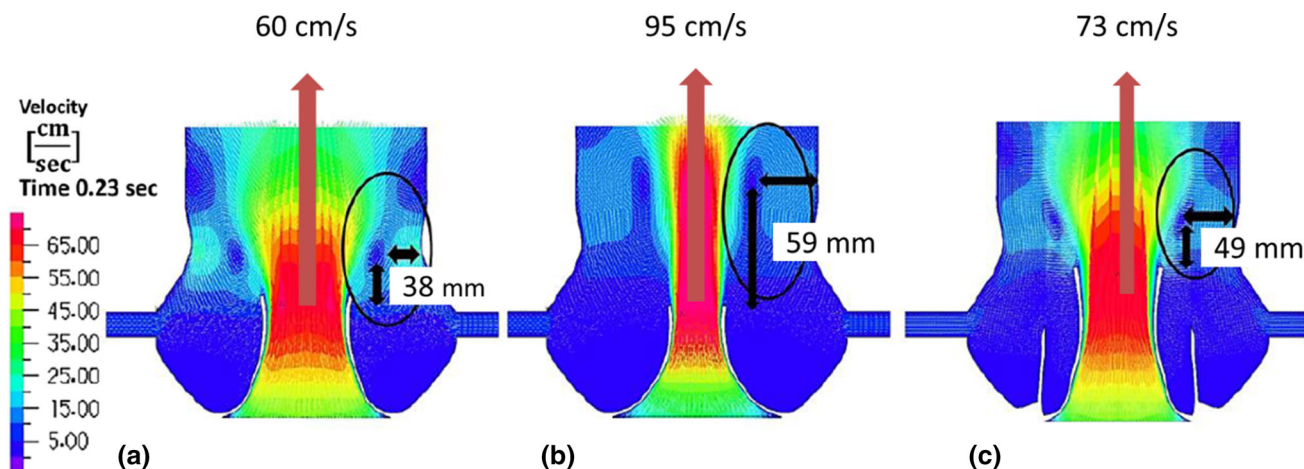
During the final period of a systolic phase, the magnitude and location of the vortical flow is varying between the five models, and a correlation is found between the peak systolic velocity through the valve orifice and the distance of the vortex downstream away from the valve (see detailed values in Table 3). Figure 14 shows three cases for example at end systolic stage ( $t = 0.23$  s). It is shown that the healthy case has the lowest systolic velocity (60 cm/s), as well as the closest vortical flow to the valve during end systole (38 mm). In the severe AS case, high peak systolic velocities are found (95 cm/s) as well as distant vortical flow during end systole (59 mm). The long TAVI case has medium systolic velocity (75 cm/s), and the vortex is located between the AS and the healthy cases (49 mm).

Between the short and long TAVI cases (Fig. 15), the systolic velocity is almost similar (the short TAVI is slightly higher); however, the leaflet configuration alters the vortices developed from the leaflet tip. In the short TAVI case, the vortex developed is stronger and located more proximal (45 mm) than in the long TAVI case (49 mm).

During the beginning of diastole, the retrograde velocity near the sinus wall increases and the center of the vor-

tex advances downstream to the aorta for all cases. At this stage, the coronary flow starts to increase due to increased pressure differences between the aorta and the coronaries ( $TPG_{ALC}$ ). In Fig. 16, pressure distribution maps of the five cases are shown at  $t = 0.15$  s,  $t = 0.26$  s and  $t = 34$  s and  $t = 0.46$  s. The time-dependent normalized aortic-coronary pressure drops ( $TPG_{ALC}$ ) for the five cases are shown in Fig. 17.

During first half of systole, pressure distribution in all cases is mainly determined by the paravalvular pressure drop (across the valve) and  $TPG_{ALC}$  is similar for all cases. Therefore, the coronary flow is similar (Fig. 11). After peak systole, vortical flow is developed and  $TPG_{ALC}$  decreases in all cases, reaching minimum at end systole. The interplay between vortex strength and location are well reflected in  $TPG_{ALC}$  values and therefore coronary flow (see a schematic description on the vorticity maps in Fig. 18). In the healthy case, the vortical flow is stronger and remains at a relatively proximal location until the beginning of diastole, resulting with low  $TPG_{ALC}$ , and thus lower coronary flow during beginning of diastole. In the severe AS case, the vortical flow is weak and is drawn downstream at an early stage,

**Fig. 14** Variation of a flow pattern at  $t = 0.23$  s for the **a** healthy model, **b** severe AS and **c** long TAVI

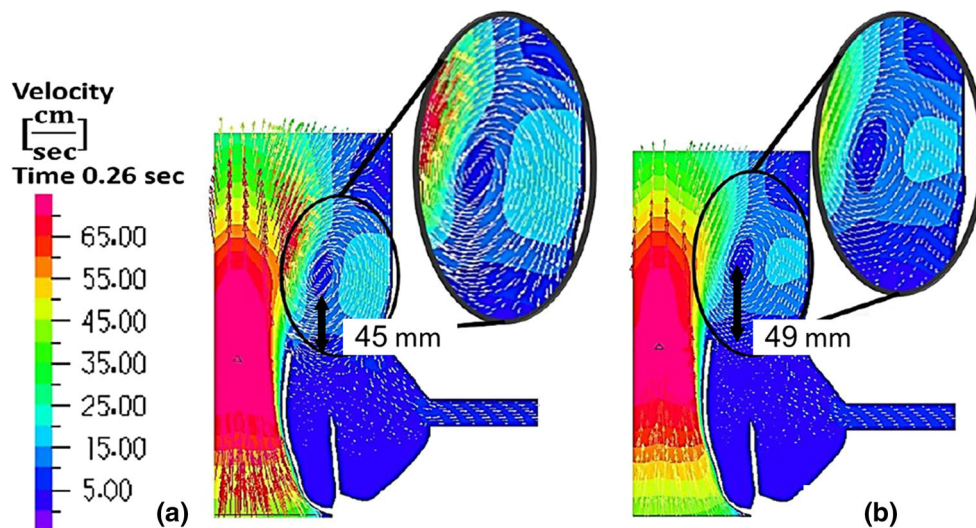


**Fig. 15** TAVI models at  $t = 0.26$  s, **a** short TAVI, stronger and closer vortex and **b** long TAVI, weaker and distant vortex

resulting with high  $TPG_{ALC}$  and thus higher coronary flow during beginning of diastole. The vortices in the TAVI cases are located relatively at proximal locations, similar to the healthy case, but they are weaker (with the weaker vortex for the long TAVI) and thus  $TPG_{ALC}$  values are relatively low during beginning of diastole.

### 3.1 Results summary

Table 4 compares the main hemodynamic results that influence the coronary flow in the five cases. Maximal systolic orifice diameter is the maximal diameter between the leaflets at peak systole. EOA is calculated according to Eq. 7. Smaller orifice diameter and EOA (like in the AS case) resulted in higher systolic velocity. Therefore, orifice diameter and EOA is correlated in Table 4 with the values of peak systolic velocity. The higher the systolic velocity, the further the vortex is washed downstream (as shown in Fig. 14); therefore, the distance of the vortex from the leaflets origin detailed in Table 4 is correlated with EOA, with farther vortex for AS cases. The vortex induces low pressure; therefore, the further the vortex is washed downstream, the higher the pressure at the coronary origin ( $P_{LC}$ ) during the beginning of diastole. This, in turn, results in higher  $TPG_{ALC}$  values. Therefore, the AS cases have higher  $TPG_{ALC}$  values than the TAVI and the healthy cases. This also affects the timing of the  $TPG_{ALC}$  peak. In AS cases, the  $TPG_{ALC}$  peak occurs earlier at the beginning of diastole, when the coronary resistance is lowest, resulting with a larger coronary flow at the beginning of diastole. This is well shown in the values of CBF and coronary flow percentage (out of the CO).

Table 4 may explain the role of vortex location and their timing on blood hemodynamics in the aortic root during the diastolic phase. In cases with high systolic velocity (such as

the severe AS), the vortices are drug downstream far from the sinus and thus the pressure in the coronary region during diastole is higher, resulting in higher coronary flow rate. This hemodynamics mechanism may shed some light on the reasons for the increase in coronary flow in AS cases during rest conditions.

## 4 Discussion

In this study, we present a numerical model that describes the transient flow in the aortic root and coronaries and compare the hemodynamic flow characteristics for five different models: a healthy valve, mild AS, severe AS, short-leaflets TAVI and long-leaflets TAVI. The simulation includes a complex combination of strong FSI coupling with large deflection, contact and gap conditions, and delicate pressure, flow and resistance time-dependent BCs.

Using comparative analyses, we illustrated the hemodynamic differences between the cases studied. The main results show that at rest conditions (CO = 3 L/min. HR = 60 BPM), the coronary flow increases with AS severity and reduces with TAVI, but not to the normal values of the healthy valve. The TAVI model with shorter leaflets had lower CBF than long TAVI leaflets.

We use flow patterns, velocity, flow rate and pressure parameters to describe the flow dynamics at each phase of the cardiac cycle and to delineate the effect of vortical structures developing leeward to the leaflets and in the sinuses on the CBF.

The results explain why the coronary flow in AS cases is higher than the healthy case, and why after TAVI there is a significant decrease of CBF, specifically during diastole.

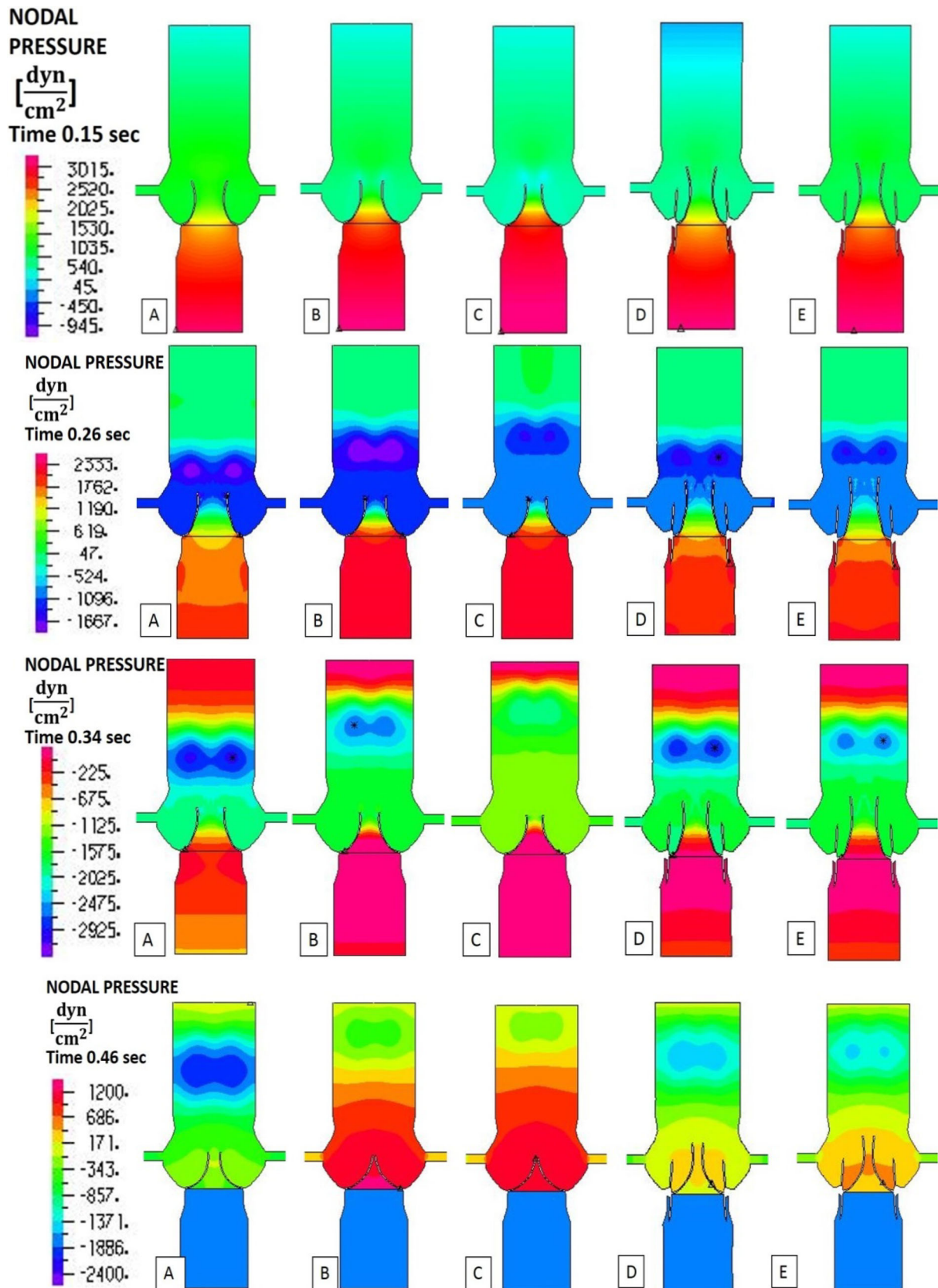


**Fig. 16** Pressure distribution at the five cases for four time instances along the cardiac cycle:  $t = 0.15$ ,  $t = 0.26$ ,  $t = 0.34$  and  $t = 0.46$ . **a** Healthy, **b** mild stenosis, **c** severe stenosis, **d** short TAVI and **e** long TAVI

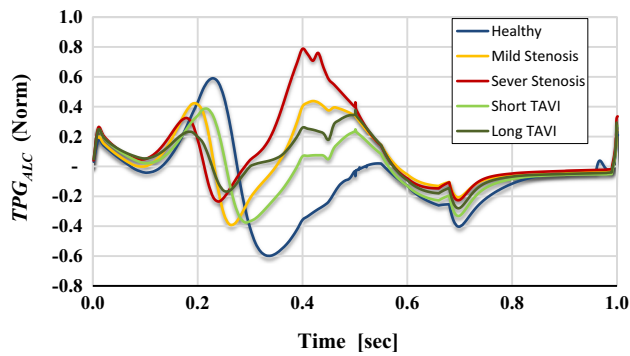


**Fig. 17** Normalized aortic-coronary pressure differences ( $TPG_{ALC}$ ) versus time, during one cardiac cycle

Our results show that the main coronary flow is dominant by the diastolic aortic-coronary pressure drop ( $TPG_{ALC}$ ). Similar to in vivo reports (Ben-Dor et al. 2009), systolic  $TPG_{ALC}$  does not change significantly for AS cases or before and after TAVI. During first half of systole, pressure distribution in all cases is mainly determined by the paravalvular pressure drop (across the valve) and is similar for all cases. The main differences are during diastole.

During the systolic phase, the flow in the aortic root is dominated by a vortex ring formed at the leaflet tip which is swept downstream with the blood stream. Evidence of the existence of such a vortex, which was first sketched by Leonardo Da Vinci (Gharib et al. 2002), has been reported in many in vitro (Peacock 1990; Querzoli et al. 2014), in vivo (Bissell et al. 2014; Kilner et al. 1993) and numeri-

cal (Sotiropoulos 2015) studies. The vortical flow and the sinus anatomy of the aortic root play two important roles in the valve operation. The vortices assist both opening and closure of the valve leaflets and ensure full opening of the valve during systole (Bellhouse 1972; Grande-Allen et al. 2000; Kvitting et al. 2004). However, these vorticities seem to be the dominant factor in decreasing the coronary flow during diastole, since they reduce the pressure drop between the aorta and the coronaries during diastole and thus reduce the coronary flow. Previous in vitro studies (Calderan et al. 2015) have shown a direct correlation between the presence of vortices and the change in pressure during that phase. Our study reveals the role of these vortices dynamics in terms of their position, strength and timing in the different cases.

In AS cases, these vortices develop at an earlier stage and at a weaker intensity than the normal case. In addition, severe AS induces higher systolic velocities that convect the vortices further downstream and thus increase in the pressure in the aortic root during diastole. This, in turn, increases the  $TPG_{ALC}$  and therefore induces higher coronary flow rates. This hemodynamics patterns may explain the higher coronary flow in the severe AS cases under rest conditions reported in previous clinical (Burwash et al. 2008; Eberli et al. 1991; Gould et al. 1976; Hongo et al. 1993; Lumley et al. 2016; Rolandi et al. 2016) and in vitro studies (Calderan et al. 2015; Gaillard et al. 2010), and also validated in an experimental study of our group (see “Appendix”).

Both TAVI models improved the systolic paravalvular pressure compared to the AS cases (similar to reported studies (Ducci et al. 2012)). They also have higher diastolic CBF

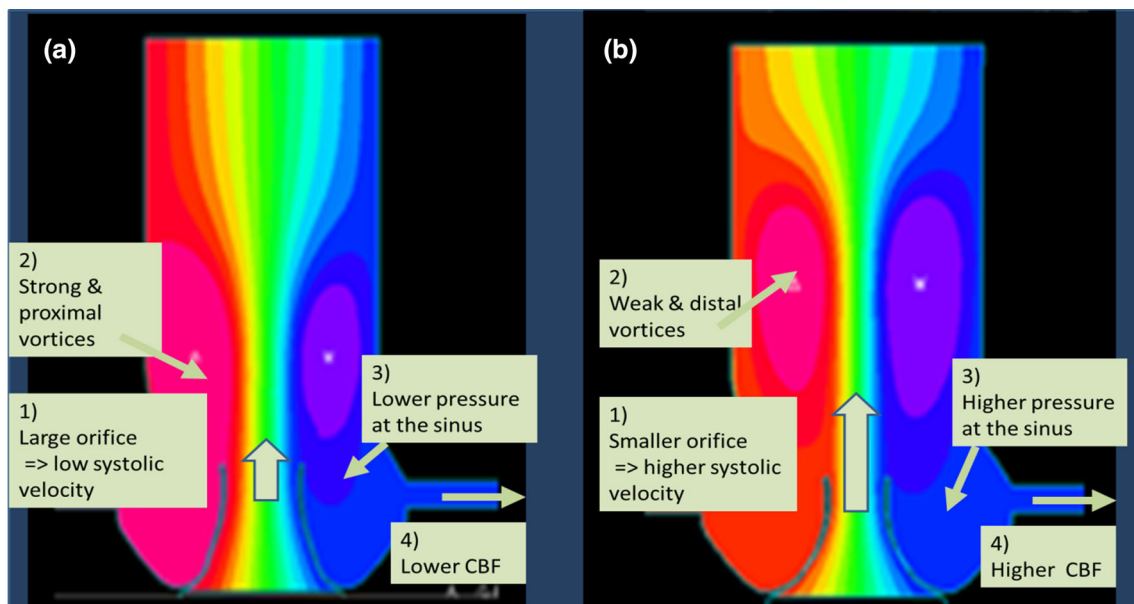


**Fig. 18** Vorticity maps at  $t = 0.3$  s for healthy (a) and AS (b) cases, with a schematic description of the interplay between orifice size and systolic velocity (1), vortex strength and location (2) local pressure values in the sinus (3) and coronary flow (4)

**Table 4** Summary of boundary conditions of the fluid domain

Systole ( $0_{\text{sec}} < t < 0.5_{\text{sec}}$ )	$V_{LV}(t)$ $P_{LV} = \tau_n^{LV}(t)$ $P_{cor} = \tau_n^{cor}(t)$	Figs. 4a and 5
Diastole ( $0.5_{\text{sec}} < t < 1_{\text{sec}}$ )	$P_{LV} = \tau_n^{LV}(t)$ $P_{cor} = \tau_n^{cor}(t)$ $R_{cor} = R_{cor}(t)$	Figs. 4b and 6

than the healthy case, similar to previous studies (Davies et al. 2011). The long TAVI has 7% more flow than the healthy and the short TAVI has only 4.5% more. This can be explained by the weaker vortices formed in the TAVI cases. The long TAVI case had weaker and distant vortex and thus higher CBF, suggesting optional design improvements by leaflets length (Bakhtiari et al. 2007).

#### 4.1 Evaluation of model assumptions

This study is aimed at comparing the overall behavior of flow in five cases (of normal, stenosis and TAVI valves) and therefore represents only a quantitative analysis to compare the different procedures. Consequently, the numerical models used several simplifications. The assumptions and simplifications that we made to solve the problem need to be carefully evaluated and their implications are discussed below.

Our main simplification is related to the 2D geometry and boundary conditions. This simplification should have a strong effect on the actual flow, since it does not consider the complex 3D geometry of the aortic root and the 3D flow structures that take place in the aortic root and downstream of the valve. The relevance of the 2D solution needs to be compared to a more elaborate 3D model or compared with the results of in vitro experiments. Such experiments were performed in parallel in our laboratory using the same geometry in a 3D model (see ‘‘Appendix’’). It was found that the major results are consistent with the in vitro model. A strong correlation in the flow pattern, flow rate and pressure drop were found supporting the findings of the 2D numerical models.

The models do not target a specific patient geometry or boundary condition. The models are based on representative prototypes of anatomical geometry constructed based anatomical database (Dvir et al. 2013; Labrosse et al. 2006; Thubrikar 1989), and the boundary conditions are based on a typical time functions garnered from the literature (Berne and Levy 1986). Since patient-specific anatomies and physiology come in large variations, whatever models we use will be inaccurate for the specific patient. However, the typical geometry we chose should be feasible for non-specific comparison analyses. For example, the coronary distance from the aortic valve for all cases were assumed to be at an equal

distance between the right and left coronaries in all the models. However, in reality, there is a change in height between the right and left coronary ostia.

In all the cases, left coronary parameters were compared using the same distance from the aortic valve. The differences between the left and right coronaries height and diameters could affect the obtained values. We also considered identical boundary conditions at the left and right coronaries. However, while this assumption might affect the absolute velocity values range, this affect should be similar for all the models. Therefore, the velocity pattern differences, pressure drops and velocity range differences between the models should still be the same. Nevertheless, we conducted a simulation of a model with a different distance of coronary ostia from the aortic valve. However, the asymmetric patterns that formed in the model (and at some level exists in reality) made the simulation very sensitive and due to software limitations, this simulation failed to converge.

The coronary resistance boundary conditions were obtained based on a typical physiological coronary blood flow measured for a healthy person at rest (Marn et al. 2012). Some assumptions have been made in setting the time-dependent distribution of resistance, like linear increase during the myocardium relaxation. This assumption is based on models of coronary wave intensity and increased myocardium dynamic elastane during diastole, as described by previous works (Kwon et al. 2014; Lee and Smith 2012). Another major assumption is that the coronary resistance was assumed to be similar for all cases, including the AS cases. This assumption was made in order to isolate the hemodynamic aspects from the physiological aspects of real cases. In actual cardiac physiology, the increase in LV pressure (expressed in our study with the parameter  $TPG_{NET}$ ) should increase the coronary resistance due to the contraction of the myocardium. This assumption is consistent with the experiment we conducted, and although it does not reflect real cardiac physiology during AS, it may help shed light on the mechanisms found in clinical tests during rest conditions.

The assumption of linear elastic material properties for the leaflets may be questionable. Physiological valve tissue is known as anisotropic and hyperelastic (Sacks and Sun 2003). Moreover, in AS valves with calcifications, the situation is even more complex, since calcifications are distributed nonuniformly over the leaflet, inducing irregular leaflet shapes and increasing the complexity of the flow patterns. Moreover, the surfaces of the leaflets become more irregular, especially on the ventricular surface of the leaflet (Yap et al. 2012). While specific studies of these phenomena have not been undertaken to date, they should be considered in assessing actual clinical flow data from stenotic valves. In our model, similar to previous studies (Grande-Allen et al. 2001), we assumed isotropic and linear elastic

material properties and the calcification was assumed to be uniform along the leaflet. Nonuniform calcification could have some effect on the results; however, the main features of flow and pressure should be similar. Furthermore, the flow in all models is driven by the same transvalvular pressure drop and the deformations of the leaflets are predicted using similar material models. These two factors should reduce the impact of the calcification nonuniformly on the leaflet tissue.

Other simplifications are related to the flow assumptions. The assumption of Newtonian fluid should be reasonable in this case. This is because the shear rates in the aorta are generally greater than  $100 \text{ s}^{-1}$  (Fung 1993). The assumption of laminar flow may have limitations, although it is considered relatively common for the aortic valve (Marom et al. 2011; Weinberg et al. 2010; Yoganathan et al. 2005). In our simulations, maximal  $Re = 2380$  and average  $Re = 700$ . These values are relatively low; however, the aortic flow may undergo a transition from a laminar to a turbulent state during the systolic deceleration phase (Bluestein and Einav 2001; Lantz et al. 2013; Weinberg et al. 2010). This transition is a challenge to model, since it is highly unstable. Low-Reynolds turbulence models, such as the Reynolds-averaged Navier–Stokes (RANS) approach with  $k-\omega$  low-Reynolds models (Schiestel 2010) or large eddy simulation (LES) (Ge et al. 2005) were developed for simple cases of boundary layer flows and does not necessarily fit complex FSI problems (Varghese et al. 2008). The more accurate option is using the direct numerical simulation (DNS), where full Navier–Stokes equations are solved without any averaging. These simulations require very fine temporal and spatial discretization and thus required high computational resources in order to ensure convergence (Dasi et al. 2007; Tullio et al. 2009; Vita et al. 2016; Nobili et al. 2008). In the current case, with direct FSI simulation, this requirement becomes extremely demanding. Due to the high demands of the FEM and the direct FSI solution, the assumption of laminar flow highly simplified the model and made the simulation possible; thus, it was inevitable. Therefore, the laminar flow was assumed.

The use of a lumped-model for coronary peripheral resistance is commonly done. However, it might add some error, since it does not incorporate the wave traveling downstream the coronary arteries. The use of gap conditions to simulate leaflet contact should not add a major error to the simulations, since the gap size is relatively small in respect with the leaflet width (0.6 cm).

In summary, the purpose of this study was to depict the major dominant factors of the aortic valve on the coronary perfusion while using a simple and feasible model. Despite the simplifications and assumptions mentioned above, the results agree with in vitro and clinical evidences regarding the effect of valve stenosis and TAVI on CBF. This simple

model may provide essential information and shed light on the hemodynamic mechanisms that determine the flow field and affect the coronary flow.

## 5 Summary and conclusions

In this study, we present a numerical model that provides a better understanding of the hemodynamic role of valve leaflets dynamics on the CBF in healthy, AS and TAVI cases. The hemodynamic mechanism provides a simple theoretical description of the correlation between orifice area, systolic blood velocity, vortices location, pressure drop and coronary flow. In the AS case, small orifice area leads to higher systolic velocities, which drag the vortices downstream further from the aortic root. This is in contrast to the healthy and TAVI cases, where the vortices are located at proximal location, near the coronary ostia, and locally reduce the aortic pressure during diastole. Thus, the diastolic pressure drop across the coronary arteries and the CBF can be easily related to the AV orifice area through this simple hemodynamic mechanism.

To demonstrate this mechanism numerically, a fully FSI coupled simulation is required. Such a simulation of a 3D anatomical-specific model is considered an extremely consuming and challenging task. In this work, we suggest a simplified 2D numerical simulation to demonstrate the main feature of the flow.

Our 2D FSI simulations succeeded to capture the dominant hemodynamic characteristics that determine the coronary flow. It allowed us to examine the impact of aortic valve stenosis and valve replacement on the coronary flow. The analysis results agree with clinical, in vivo, in vitro and experimental results, and it provides an important insight and emphasizes the need for more comprehensive studies on coronary's hemodynamics after valve replacement. There are numerous variations of TAVI designs, and it is very difficult and time-consuming to cover all the possible models. Since CBF can be influenced by the valve size and design (Ben-Dor et al. 2014; Kopanidis et al. 2015), the uses of a 2D model with FSI and varying coronary resistance can be of great help to demonstrate the main features of the design.

**Acknowledgements** This work was conducted in Ariel Biomechanics Center (ABMC) in Ariel University. Shaily Wald was supported by scholarship provided by Ariel University. The research was partially supported by a grant from the Nicholas and Elizabeth Slezak Super Center for Cardiac Research and Biomedical Engineering at Tel Aviv University, in collaboration with Prof. Ran Kornowski, Rabin Medical Center.

### Compliance with ethical standards

**Conflict of interest** The authors declare that they have no conflict of interest.

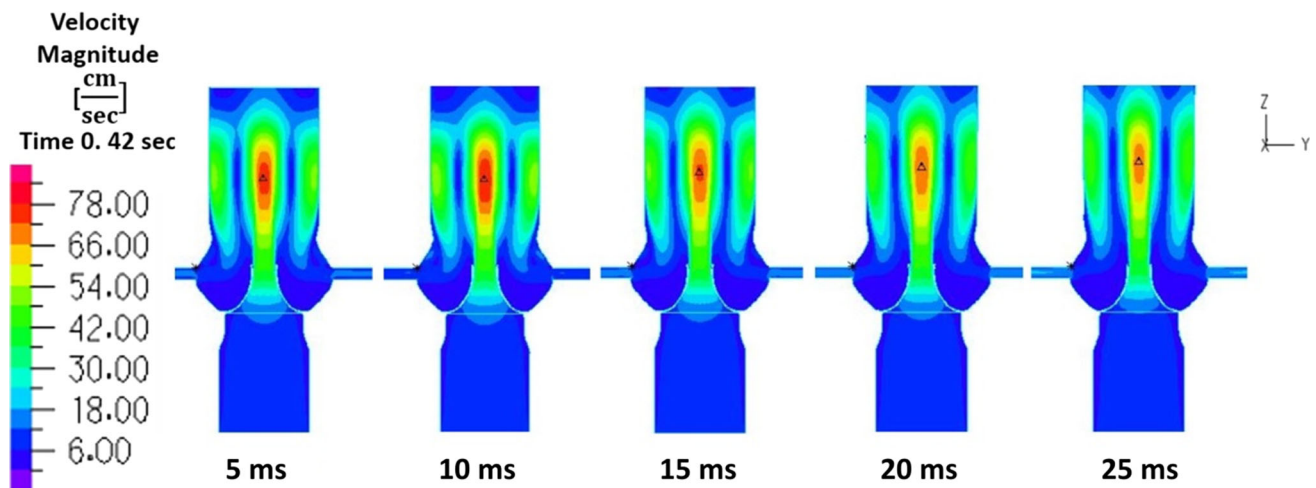


**Fig. 19** velocity magnitude for the different time steps intervals at time 0.42 s

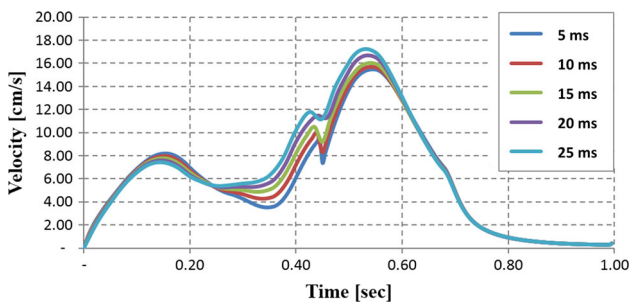


**Fig. 20** Time-dependent average coronary velocity for the different time steps intervals

**Table 5** Details of the time step intervals, calculation time and average relative difference

Time step size (ms)	Total no. of steps	CPU time (s)	Average relative difference (%)
5	601	23,921	0
10	551	8254	1.5
15	525	7155	3.5
20	523	6993	8
25	521	6778	11

## 6 Appendix

### Model validation

#### Time step independence tests

Mesh and time step independence tests were conducted to validate the numerical model. To evaluate the optimal time step size for the transient simulations, simulations of the healthy case with the mesh of 30,000 nodes were performed using 5 different time step intervals of  $dt = 5, 10, 15, 20$  and  $25$  ms. The resulted velocity magnitude for the different time steps intervals are shown in Fig. 19 corresponding to  $t = 0.42$  s.

For all the cases, at  $t = 0.5$  s, the time step is reduced to  $dt = 1$  ms to allow converge at the delicate stage of valve closure. Figure 20 shows a comparison of the average coronary velocity during the cardiac cycle for the five cases of time step resolutions.

To evaluate the discretization error, we calculated the relative difference (ERR) between the average coronary flow of

each case and the finest time resolution case, as follows:

$$ERR_i [\%] = \int_T \left( \frac{(V_y)_{finest} - (V_y)_i}{(V_y)_{finest}} \right) dt * 100 [\%] \quad (\text{A.1})$$

where  $V_y$  is the time-dependent average coronary velocity (as described by Eq. 5) and  $T$  is the cycle period. Table 5 details the average ERR of the different cases. The results show that the time step of  $dt = 10$  ms is sufficient during systole, with  $ERR = 1.5\%$ . During diastole ( $t > 0.5$  s), steps of 1 ms were used to allow convergence. Therefore, for the transient analyses in this study, 551 steps were set per cycle.

#### Mesh independence tests

To evaluate the optimal mesh resolution, five models of the healthy base case with different mesh resolutions were built (with 20,000–60,000 nodes). The models were simulated during a period of one cardiac cycle. Figure 21 shows a comparison of the average coronary velocity during the cardiac cycle for the five mesh resolutions and Table 6 details the average relative differences of the different cases. Based on



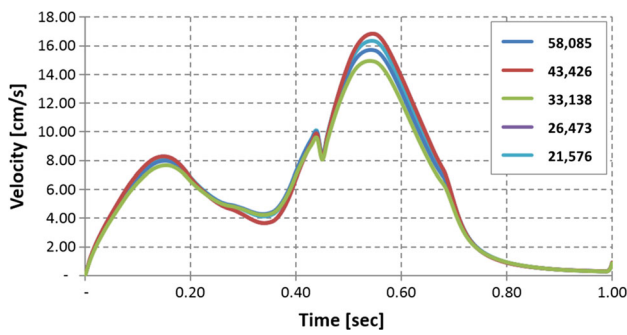


**Fig. 21** Time-dependent average coronary velocity for the different mesh models (number of nodes)

**Table 6** Details of mesh models, calculation time and average relative difference

No. of nodes	No. of elements	CPU time (s)	Average relative difference (%)
58,085	63,596	14,300	0
43,426	47,551	9267	2
33,138	36,009	8254	4
26,473	28,666	4063	5
21,576	23,184	4735	6

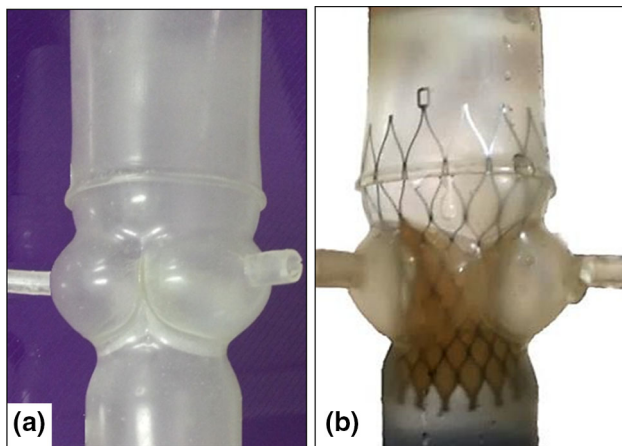


**Fig. 22** Experimental models, **a** healthy/AS; **b** TAVI

these results, mesh resolutions of 30,000 nodes were found suitable for our model with ERR = 4% of the finest mesh.

*Comparison with in vitro results*

The numerical study was conducted in parallel to an experimental study that was performed by another member in our group (to be published in a future publication). The study included a healthy, AS and TAVI in vitro models with similar characteristics as the numerical model described here (Fig. 22). The flow was driven by a pulsatile piston pump which was synchronized with a controlled coronary arteries

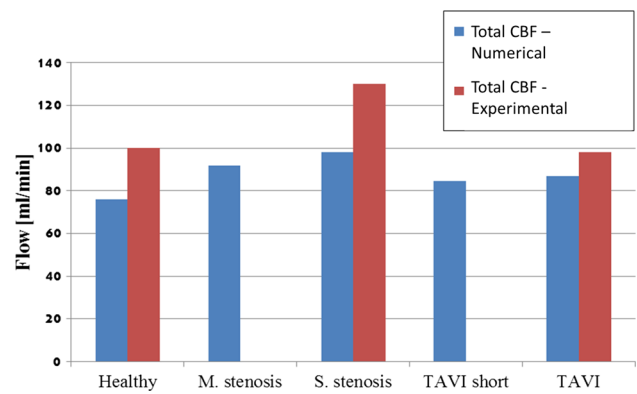


**Fig. 23** Coronary flow rate for the different cases in the numerical (blue) and experimental (red) models

resistance. Similar working conditions (HR and CO) were used. Measurement of coronary flow rates are shown as red columns in Fig. 23. Although only one AS model (severe AS) and one TAVI model (the long TAVI) were modeled in the in vitro study, the experimental results agree with the numerical results. AS case showed higher coronary flow than healthy case, and TAVI leads to normalization of the coronary flow.

**References**

ADINA R&D I (2000) ADINA theory and modeling guide vol Volumes I, II and III. Watertown, MA

Ahn J-H et al (2016) Coronary microvascular dysfunction as a mechanism of angina in severe AS: prospective adenosine-stress CMR study. *J Am Coll Cardiol* 67:1412–142

Avrahami I (2012) Cardiovascular vortex in numerical simulations. In: Kheradvar A, Pedrizzetti G (eds) *Vortex formation in cardiovascular system*. Springer, Berlin

Bakhtiyari F et al (2007) Impact of patient–prosthesis mismatch and aortic valve design on coronary flow reserve after aortic valve replacement. *J Am Coll Cardiol* 49:790–796

Bathe K-J (2006) *Finite element procedures*. Klaus-Jurgen Bathe, Berlin

Bellhouse B (1972) The fluid mechanics of heart valves. In: Bergel DH (ed) *Cardiovascular fluid dynamics*. Academic Press, London

Ben-Dor I et al (2009) Effects of percutaneous aortic valve replacement on coronary blood flow assessed with transesophageal Doppler echocardiography in patients with severe aortic stenosis. *Am J Cardiol* 104:850–855

Ben-Dor I et al (2014) Coronary blood flow in patients with severe aortic stenosis before and after transcatheter aortic valve implantation. *Am J Cardiol* 114:1264–1268

Berne R, Levy M (1986) *Cardiovascular physiology*. Mosby, St. Louis

PN Watton et al. *J Fluids Struct* 24 (2008) 58 74:72

Bertrand ME, Lablanche JM, Tilmant PY, Thieuleux FP, Delforge MR, Carré AG (1981) Coronary sinus blood flow at rest and during isometric exercise in patients with aortic valve disease: mechanism of angina pectoris in presence of normal coronary arteries. *Am J Cardiol* 47:199–205

Bianchi M, Ghosh RP, Marom G, Slepian MJ, Bluestein D (2015) Simulation of transcatheter aortic valve replacement in patient-specific aortic roots: effect of crimping and positioning on device performance. In: *Engineering in Medicine and Biology Society (EMBC)*,

- 2015 37th annual international conference of the IEEE, IEEE, pp 282–285
- Bissell MM, Dall' Armellina E, Choudhury RP (2014) Flow vortices in the aortic root: in vivo 4D-MRI confirms predictions of Leonardo da Vinci European heart journal:ehu011
- Bluestein D, Einav S (2001) Techniques in the stability analysis of pulsatile flow through heart valves. In: Leonides Cornelius T (ed) Cardiovascular techniques, biomechanical systems. techniques and applications. CRC Press, Boca Raton
- Borazjani I (2013) Fluid-structure interaction, immersed boundary-finite element method simulations of bio-prosthetic heart valves. *Computer Methods in Applied Mechanics and Engineering* 257:103–116
- Broyd CJ, Sen S, Mikhail GW, Francis DP, Mayet J, Davies JE (2013) Myocardial ischemia in aortic stenosis: insights from arterial pulse-wave dynamics after percutaneous aortic valve replacement. *Trends Cardiovasc Med* 23:185–191
- Burwash IG et al (2008) Myocardial blood flow in patients with low-flow, low-gradient aortic stenosis: differences between true and pseudo-severe aortic stenosis Results from the multicentre TOPAS (Truly or Pseudo-Severe Aortic Stenosis). *Study Heart* 94:1627–1633
- Calderan J, Mao W, Sirois E, Sun W (2015) Development of an in vitro model to characterize the effects of transcatheter aortic valve on coronary artery flow. *Artif Org* 40:612–619
- Camici PG, Olivetto I, Rimoldi OE (2012) The coronary circulation and blood flow in left ventricular hypertrophy. *J Mol Cell Cardiol* 52:857–864
- Cao C, Virk S, Liou K, Pathan F, Wilcox C, Novis E, Yan T (2015) A systematic review and meta-analysis of clinical and cost-effective outcomes of transcatheter aortic valve implantation versus surgical aortic valve replacement *Heart. Lung Circ* 24:S258
- Carroll R, Falsetti H (1976) Retrograde coronary artery flow in aortic valve disease. *Circulation* 54:494–499
- Christie GW, Barratt-Boyes BG (1995) Age-dependent changes in the radial stretch of human aortic valve leaflets determined by biaxial testing. *Ann Thorac Surg* 60:S156–S159
- Danson E, Hansen P, Sen S, Davies J, Meredith I, Bhindi R (2016) Assessment, treatment, and prognostic implications of CAD in patients undergoing TAVI. *Nat Rev Cardiol* 13:276
- Dasi L, Ge L, Simon H, Sotiropoulos F, Yoganathan A (2007) Vorticity dynamics of a bileaflet mechanical heart valve in an axisymmetric aorta. *Phys Fluids* 19:067105
- Davies JE et al (2011) Arterial pulse wave dynamics after percutaneous aortic valve replacement fall in coronary diastolic suction with increasing heart rate as a basis for angina symptoms in aortic stenosis. *Circulation* 124:1565–1572
- De Tullio MD, Cristallo A, Balaras E, Verzicco R (2009) Direct numerical simulation of the pulsatile flow through an aortic bileaflet mechanical heart valve. *J Fluid Mech* 622:259–290
- De Vita F, de Tullio M, Verzicco R (2016) Numerical simulation of the non-Newtonian blood flow through a mechanical aortic valve. *Theor Comput Fluid Dyn* 30:129–138
- Doyle MG, Tavoularis S, Bourgault Y (2010) Application of parallelprocessing to the simulation of heart mechanics. In: Mewhort DJK (ed) High performance computing systems and applications, Springer, Berlin, pp 30–47
- Ducci A, Tzamtzis S, Mullen M, Burriesci G (2012) Phase-resolved velocity measurements in the Valsalva sinus downstream of a Transcatheter Aortic Valve. In: 16th International symposium on applications of laser techniques to fluid mechanics, Lisbon, Portugal, pp 9–12
- Dvir D et al (2012) Multicenter evaluation of Edwards SAPIEN positioning during transcatheter aortic valve implantation with correlates for device movement during final deployment. *JACC Cardiovasc Interv* 5(5):563–570
- Dvir D, Lavi I, Kornowski R (2013) Transcatheter aortic valve implantation of a Core Valve device using novel real-time imaging guidance. *Cardiovasc Revascularization Med* 14(1):49–52
- Eberli F, Ritter M, Schwitzer J, Bortone A, Schneider J, Hess O, Krayenbuehl H (1991) Coronary reserve in patients with aortic valve disease before and after successful aortic valve replacement. *Eur Heart J* 12:127–138
- Fung YC (1993) Biomechanics: mechanical properties of living tissues. Springer, Berlin
- Gaillard E, Garcia D, Kadem L, Pibarot P, Durand L-G (2010) In vitro investigation of the impact of aortic valve stenosis severity on left coronary artery flow. *J Biomech Eng* 132:044502
- Garcia D, Camici PG, Durand L-G, Rajappan K, Gaillard E, Rimoldi OE, Pibarot P (2009) Impairment of coronary flow reserve in aortic stenosis. *J Appl Physiol* 106:113–121
- Garcia D, Kadem L, Savéry D, Pibarot P, Durand L-G (2006) Analytical modeling of the instantaneous maximal transvalvular pressure gradient in aortic stenosis. *J Biomech* 39:3036–3044
- Ge L, Leo HL, Sotiropoulos F, Yoganathan AP (2005) Flow in a mechanical bileaflet heart valve at laminar and near-peak systole flow rates: CFD simulations and experiments. *J Biomech Eng Trans ASME* 127:782–797
- Ge L, Sotiropoulos F (2010) Direction and magnitude of blood flow shear stresses on the leaflets of aortic valves: is there a link with valve calcification? *J Biomech Eng Trans ASME* 132:014505
- Gharib M, Kremers D, Koochesfahani M, Kemp M (2002) Leonardo's vision of flow visualization. *Exp Fluids* 33:219–223
- Gilmanov A, Le TB, Sotiropoulos F (2015) A numerical approach for simulating fluid structure interaction of flexible thin shells undergoing arbitrarily large deformations in complex domains. *J Comput Phys* 300:814–843
- Gould K, Lipscomb K, Hamilton G, Kennedy J (1976) Retrograde coronary artery flow in aortic valve disease. *Circulation* 54:494–499
- Gould KL, Carabello BA (2003) Why angina in aortic stenosis with normal coronary arteriograms? *Circulation* 107:3121–3123
- Gould KL, Johnson NP (2016a) Imaging coronary blood flow in AS: let the data talk. *Again J Am Coll Cardiol* 67:1423–1426
- Gould KL, Johnson NP (2016b) Ischemia in aortic stenosis: new insights and potential clinical relevance. *J Am Coll Cardiol* 68:698–701
- Grande-Allen KJ, Cochran RP, Reinhall PG, Kunzelman KS (2000) Re-creation of sinuses is important for sparing the aortic valve: a finite element study. *J Thorac Cardiovasc Surg* 119:753–763
- Grande-Allen KJ, Cochran RP, Reinhall PG, Kunzelman KS (2001) Finite-element analysis of aortic valve-sparing: influence of graft shape and stiffness. *IEEE Trans Biomed Eng* 48:647–659
- Griffith BE (2012) Immersed boundary model of aortic heart valve dynamics with physiological driving and loading conditions. *Int J Numer Methods Biomed Eng* 28:317–345
- Hongo M et al (1993) Relation of phasic coronary flow velocity profile to clinical and hemodynamic characteristics of patients with aortic valve disease. *Circulation* 88:953–960
- Julius BK, Spillmann M, Vassalli G, Villari B, Eberli FR, Hess OM (1997) Angina pectoris in patients with aortic stenosis and normal coronary arteries mechanisms and pathophysiological concepts. *Circulation* 95:892–898
- Kelly TA, Rothbart RM, Cooper CM, Kaiser DL, Smucker ML, Gibson RS (1988) Comparison of outcome of asymptomatic to symptomatic patients older than 20 years of age with valvular aortic stenosis. *Am J Cardiol* 61:123–130
- Kilner PJ, Yang GZ, Mohiaddin RH, Firmin DN, Longmore DB (1993) Helical and retrograde secondary flow patterns in the aortic arch studied by three-directional magnetic resonance velocity mapping. *Circulation* 88:2235–2247
- Kim HJ, Vignon-Clementel IE, Coogan JS, Figueroa CA, Jansen KE, Taylor CA (2008) Patient-specific modeling of blood flow and

- pressure in human coronary arteries. *Ann Biomed Eng* 38:3195–3209
- Klabunde R (2011) *Cardiovascular physiology concepts*. Lippincott Williams and Wilkins, Philadelphia
- Kolh P et al (2014) 2014 ESC/EACTS guidelines on myocardial revascularization the task force on myocardial revascularization of the European Society of Cardiology (ESC) and the European Association for Cardio-Thoracic Surgery (EACTS) developed with the special contribution of the European Association of Percutaneous Cardiovascular Interventions (EAPCI). *Eur J Cardio-Thorac Surg* 46:517–592
- Kopanidis A, Pantos I, Alexopoulos N, Theodorakakos A, Efstathiopoulos E, Katritsis D (2015) Aortic flow patterns after simulated implantation of transcatheter aortic valves. *Hell J Cardiol* 56:418–428
- Kupari M et al (1992) Exclusion of coronary artery disease by exercise thallium-201 tomography in patients with aortic valve stenosis. *Am J Cardiol* 70:635–640
- Kvitting J-PE, Ebbers T, Wigström L, Engvall J, Olin CL, Bolger AF (2004) Flow patterns in the aortic root and the aorta studied with time-resolved, 3-dimensional, phase-contrast magnetic resonance imaging: implications for aortic valve-sparing surgery. *J Thorac Cardiovasc Surg* 127:1602–1607
- Kwon S-S et al (2014) A novel patient-specific model to compute coronary fractional flow reserve. *Prog Biophys Mol Biol* 116:48–55
- Labrosse MR, Beller CJ, Robicsek F, Thubrikar MJ (2006) Geometric modeling of functional trileaflet aortic valves: development and clinical applications. *J Biomech* 39:2665–2672
- Lantz J, Ebbers T, Engvall J, Karlsson M (2013) Numerical and experimental assessment of turbulent kinetic energy in an aortic coarctation. *J Biomech* 46:1851–1858
- Le TB, Gilmanov A, Sotiropoulos F (2013) High resolution simulation of tri-leaflet aortic heart valve in an idealized aorta. *J Med Dev* 7:030930
- Lee J, Nordsletten D, Cookson A, Rivolo S, Smith N (2016) In silico coronary wave intensity analysis: application of an integrated one-dimensional and poromechanical model of cardiac perfusion. *Biomech Model Mechanobiol* 15:1535–1555
- Lee J, Smith NP (2012) The multi-scale modelling of coronary blood flow. *Ann Biomed Eng* 40:2399–2413
- Lumley M et al (2016) Coronary physiology during exercise and vasodilation in the healthy heart and in severe aortic stenosis. *J Am Coll Cardiol* 68:688–697
- Mahmood F, Swaminathan M (2010) *Stuck With a Decision: What Is the “True” aortic valve area—atomic, geometric, or effective orifice area?*. WB Saunders, Philadelphia
- Marcus ML, Doty DB, Hiratzka LF, Wright CB, Eastham CL (1982) Decreased coronary reserve: a mechanism for angina pectoris in patients with aortic stenosis and normal coronary arteries. *New Engl J Med* 307:1362–1366
- Marn J, Iljaž J, Žunič Z, Ternik P (2012) Non-Newtonian blood flow around healthy and regurgitated aortic valve with coronary blood flow involved. *Strojniški vestnik. J Mech Eng* 58:482–491
- Marom G, Haj-Ali R, Raanani E, Schäfers H-J, Rosenfeld M (2011) A fluid–structure interaction model of the aortic valve with coaptation and compliant aortic root. *Med Biol Eng Comput Sci Eng* 50:173–182
- Marom G, Haj-Ali R, Raanani E, Schäfers H-J, Rosenfeld M (2012) A fluid–structure interaction model of the aortic valve with coaptation and compliant aortic root. *Med Biol Eng Comput* 50:173–182
- McQueen DM, Peskin CS (2000) A three-dimensional computer model of the human heart for studying cardiac fluid dynamics. *Comput Gr Us* 34:56–60
- Meimoun P et al (2012) Factors associated with noninvasive coronary flow reserve in severe aortic stenosis. *J Am Soc Echocardiogr* 25:835–841
- Miller JD, Weiss RM, Heistad DD (2011) Calcific aortic valve stenosis: methods, models, and mechanisms. *Circ Res* 108:1392–1412
- Nicosia M, Cochran R, Einstein D, Rutland C, Kunzelman K (2003) A coupled fluid–structure finite element model of the aortic valve and root. *J Heart Valve Dis* 12:781–789
- Nobari S, Mongrain R, Leask R, Cartier R (2013) The effect of aortic wall and aortic leaflet stiffening on coronary hemodynamic: a fluid–structure interaction study. *Med Biol Eng Comput* 51:923–936
- Nobili M et al (2008) Numerical simulation of the dynamics of a bileaflet prosthetic heart valve using a fluid–structure interaction approach. *J Biomech* 41:2539–2550
- Omran H, Fehske W, Rabahieh R, Hagendorff A, Lüderitz B (1996) Relation between symptoms and profiles of coronary artery blood flow velocities in patients with aortic valve stenosis: a study using transoesophageal Doppler echocardiography. *Heart* 75:377–383
- Paradis J-M et al (2014) Aortic stenosis and coronary artery disease: What do we know? What don’t we know? A comprehensive review of the literature with proposed treatment algorithms. *Eur Heart J* 35:2069–2082
- Peacock JA (1990) An in vitro study of the onset of turbulence in the sinus of Valsalva. *Circ Res* 67:448–460
- Petropoulakis PN, Kyriakidis MK, Tentolouris CA, Kourouclis CV, Toutouzas PK (1995) Changes in phasic coronary blood flow velocity profile in relation to changes in hemodynamic parameters during stress in patients with aortic valve stenosis. *Circulation* 92:1437–1447
- Querzoli G, Fortini S, Espa S, Costantini M, Sorgini F (2014) Fluid dynamics of aortic root dilation in Marfan syndrome. *J Biomech* 47:3120–3128
- Rajappan K, Rimoldi OE, Camici PG, Bellenger NG, Pennell DJ, Sheridan DJ (2003) Functional changes in coronary microcirculation after valve replacement in patients with aortic stenosis. *Circulation* 107:3170–3175
- Rajappan K, Rimoldi OE, Dutka DP, Ariff B, Pennell DJ, Sheridan DJ, Camici PG (2002) Mechanisms of coronary microcirculatory dysfunction in patients with aortic stenosis and angiographically normal coronary arteries. *Circulation* 105:470–476
- Rolandi MC et al (2016) Transcatheter replacement of stenotic aortic valve normalizes cardiac–coronary interaction by restoration of systolic coronary flow dynamics as assessed by wave intensity analysis. *Circ Cardiovasc Interv* 9:e002356
- Rosenhek R et al (2010) Natural history of very severe aortic stenosis. *Circulation* 121:151–156
- Sacks MS, Sun W (2003) Multiaxial mechanical behavior of biological materials. *Annu Rev Biomed Eng* 5:251–284
- Scalone G, Niccoli G (2015) A focus on the prognosis and management of ischemic heart disease in patients without evidence of obstructive coronary artery disease. *Expert Rev Cardiovasc Ther* 13:1031–1044. doi:10.1586/14779072.2015.1077114
- Schiestel R (2010) *Modeling and simulation of turbulent flows*, vol 4. Wiley, Hoboken
- Schultz CJ et al (2009) Geometry and degree of apposition of the CoreValve ReValving system with multislice computed tomography after implantation in patients with aortic stenosis. *J Am Coll Cardiol* 54:911–918
- Sen S, Davies JE (2015) Demystifying Complex Coronary Hemodynamics in Patients Undergoing Transcatheter Aortic Valve Replacement Sowing the Seeds for Coronary Physiological Assessment in the Future? *Circ Cardiovasc Interv* 8:e002909
- Sotiropoulos F (2015) Fluid mechanics of heart valves and their replacements. *Annu Rev Fluid Mech* 48:259–283
- Sotiropoulos F, Borazjani I (2009) A review of state-of-the-art numerical methods for simulating flow through mechanical heart valves. *Med Biol Eng Comput* 47:245–256

- Stefanadis C, Wooley C, Bush C, Kolibash A, Boudoulas H (1988) Aortic distensibility in post-stenotic aortic dilatation: the effect of co-existing coronary artery disease. *J Cardiol* 18:189–195
- Stefanini G, Storcky S, Wenaweser P, Windecker S (2014) Coronary artery disease in patients undergoing TAVI: why, what, when and how to treat *EuroIntervention: journal of EuroPCR in collaboration with the Working Group on Interventional Cardiology of the European Society of Cardiology* 10:U69–75
- Thubrikar MJ (1989) *The aortic valve*. CRC Press, Boca Raton
- Varghese SS, Frankel SH, Fischer PF (2008) Modeling transition to turbulence in eccentric stenotic flows. *J Biomech Eng* 130:014503–014507. doi:[10.1115/1.2800832](https://doi.org/10.1115/1.2800832)
- Weinberg EJ, Mack PJ, Schoen FJ, García-Cardeña G, Mofrad MRK (2010) Hemodynamic environments from opposing sides of human aortic valve leaflets evoke distinct endothelial phenotypes in vitro. *Cardiovasc Eng* 10:5–11
- Weinberg EJ, Schoen FJ, Mofrad MR (2009) A computational model of aging and calcification in the aortic heart valve. *PLoS ONE* 4:e5960
- Wiegerinck EM et al (2015) Impact of aortic valve stenosis on coronary hemodynamics and the instantaneous effect of transcatheter aortic valve implantation. *Circ Cardiovasc Interv* 8:e002443
- Yap CH, Saikrishnan N, Tamilselvan G, Yoganathan AP (2012) Experimental measurement of dynamic fluid shear stress on the aortic surface of the aortic valve leaflet. *Biomech Model Mechanobiol* 11:171–182
- Yoganathan AP, Chandran KB, Sotiropoulos F (2005) Flow in prosthetic heart valves: state-of-the-art and future directions. *Ann Biomed Eng* 33:1689–1694
- Zhang H, Bathe K-J (2001) Direct and iterative computing of fluid flows fully coupled with structures. In: Bathe KJ (ed), *Computational fluid and solid mechanics*. Elsevier, Amsterdam
- Zingone B (2008) Impaired coronary flow reserve with aortic stenosis despite aortic valve replacement. *J Cardiovasc Med* 9:869–871